

## Supporting Information

# Ultrafast and Highly Sensitive Chemically Functionalized Graphene Oxide Based Humidity Sensors: Harnessing the Device Performances via the Supramolecular Approach

Cosimo Anichini<sup>1</sup>, Alessandro Aliprandi<sup>1</sup>, Sai Manoj Gali<sup>2</sup>, Fabiola Liscio<sup>3</sup>, Vittorio Morandi<sup>3</sup>,  
Andrea Minoia<sup>2</sup>, David Beljonne<sup>2,\*</sup>, Artur Ciesielski<sup>1,\*</sup> and Paolo Samorì<sup>1,\*</sup>

<sup>1</sup> *Université de Strasbourg, CNRS, ISIS, 8 allée Gaspard Monge, 67000 Strasbourg, France.*

<sup>2</sup> *CMN, Université de Mons, Place du Parc 20, 7000 Mons, Belgium.*

<sup>3</sup> *Istituto per la Microelettronica e Microsistemi (IMM) - CNR, via Gobetti 101, 40129 Bologna, Italy.*

\*Corresponding Authors

A. Ciesielski, P. Samorì - [ciesielski@unistra.fr](mailto:ciesielski@unistra.fr), [samori@unistra.fr](mailto:samori@unistra.fr)

D. Beljonne – [david.beljonne@umons.ac.be](mailto:david.beljonne@umons.ac.be)

**Abstract:** Humidity sensors are gaining attention because of their relevance for well-being. Within the race for new cost-efficient materials with superior performances, graphene oxide (GO) based humidity sensors are emerging because of their low-cost and high sensitivity. However, current GO-based sensors suffer from some important drawbacks such as slow response and recovery, and poor stability. Interestingly, reduced GO (rGO) exhibits higher stability, yet accompanied by a lower sensitivity to humidity due to its hydrophobic nature. With the aim of improving the sensing performances of rGO, here we report on a novel generation of humidity sensors based on a simple chemical modification of rGO with selective receptors of water molecules, i.e. triethylene glycol chains. Such hybrid material exhibits a notably improved sensing performance compared to pristine rGO such as high sensitivity (31 % increase in electrical resistance when humidity is shifted from 2 to 97%), an ultrafast response (25 ms) and recovery in the sub-second timescale, low hysteresis (1.1 %), excellent repeatability and stability as well as high selectivity towards moisture.

## Table of Contents

Instrumental methods .....	S3
Results and Discussion .....	S4
XPS .....	S4
Estimation of the functionalization grade by XPS.....	S6
Raman.....	S7
UV-Vis Transmittance Spectroscopy.....	S7
Infrared spectroscopy analysis .....	S7
Thermogravimetric analysis.....	S8
Scanning Electron Microscopy (SEM) characterization .....	S9
Atomic Force Microscopy (AFM) characterization.....	S9
Contact Angle.....	S10
Humidity sensing and VOC sensing .....	S10
Interlayer spacing vs relative humidity .....	S14
Molecular Dynamics simulations .....	S15
<sup>1</sup> H NMR of the molecule NTEG .....	S20
References.....	S20

## Instrumental methods

The X-Ray Photoelectron Spectroscopy (XPS) measurements were carried out using a Thermo Scientific KAlpha X-ray Photoelectron Spectrometer system equipped with an Al K $\alpha$  X-Ray source (photon energy  $E_{ph} = 1486.6$  eV, beam spot size  $\sim 100$   $\mu\text{m}$ ). Transmittance UV-Vis spectra were recorded on the Jasco V-670 spectrophotometer. Raman spectra were recorded by a Renishaw microscope with a 50x objective, laser excitation wavelength of 532 nm and laser power of 1%. The silicon peak at  $520.3\text{ cm}^{-1}$  was taken as reference for wavenumber calibration. The FTIR-ATR measures were performed with a Thermo Scientific Nicolet 6700 FT-IR spectrometer. TGA was conducted using a Mettler Toledo TGA/DSC 2 system, with a heating rate of  $10\text{ }^{\circ}\text{C min}^{-1}$  from  $25\text{ }^{\circ}\text{C}$  to  $800\text{ }^{\circ}\text{C}$  under argon atmosphere. The X-Ray Diffraction (XRD) measurements were performed in specular geometry using a SmartLab-Rigaku diffractometer equipped with a rotating anode (Cu K $\alpha$ ,  $\lambda = 1.54180\text{ \AA}$ ), followed by a parabolic mirror to collimate the incident beam, and a series of variable slits (placed before and after the sample position). The sample was mounted inside a box having two Kapton windows to let pass the incident and diffracted beam through and a thermoigrometer to measure RH and temperature in real time. RH was varied by changing the hydration of nitrogen flux inside the box. The flux rate was fixed to maintain the pressure constant. The water contact angle measurements were performed with a Krüss DSA100S instrument by depositing on spray-coated films of rCMGO-1, rCMGO-2 and rGO on glass 5 sessile drops of water (for each sample and performing 5 consecutive measurements (2 s delay) for each drop. For each sample, the 25 drop images were fitted by the Ellipse (Tangent-1) method and the mean values and standard deviation were reported. Atomic force microscopy (AFM) characterization of the devices was performed with a Bruker Dimension Icon microscope under ambient conditions, operating in tapping mode and using TESPA-V2 tips with spring constant  $k = 42\text{ N/m}$ . The thickness of the spray-coated materials was calculated by leveling at 0 nm the substrate and calculating the average height of the image after subtracting the substrate area. Scanning Electron Microscopy (SEM) was performed with a FEI Quanta 250 FEG instrument, operated in high vacuum mode (pressure in  $10^{-4}$  Pa range).

## Results and Discussion

### XPS

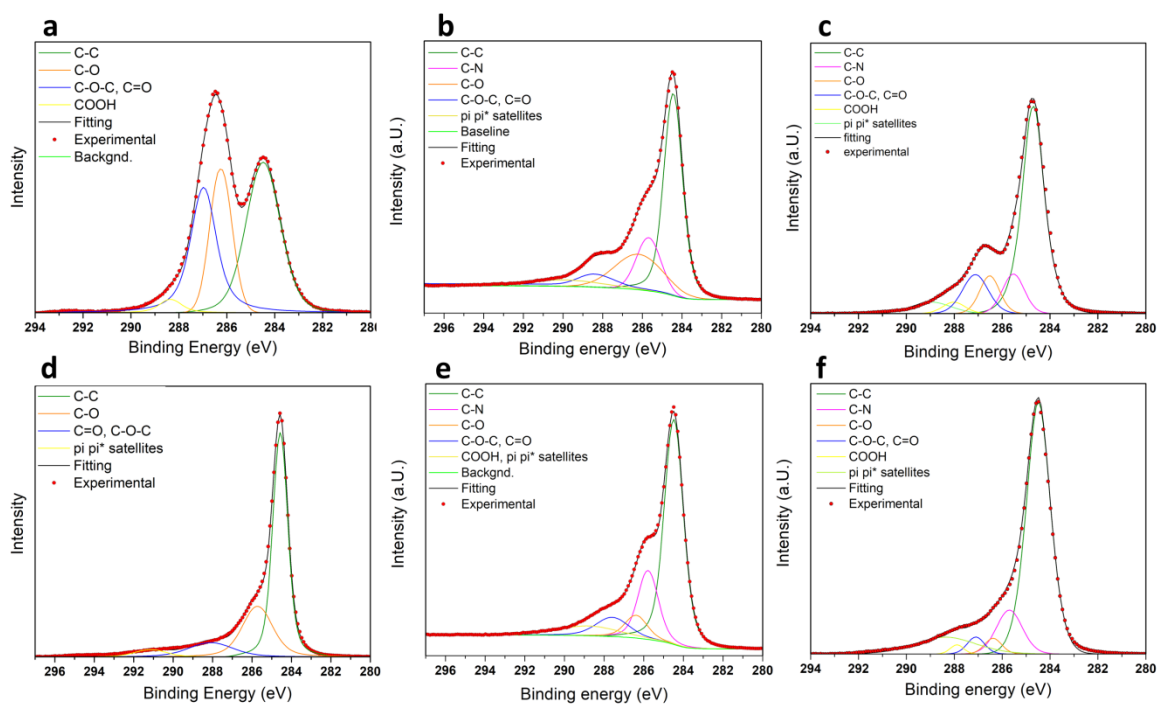


**Figure S1.** XPS spectra of C1s peaks of GO (a), CMGO-1 (b), CMGO-2 (c) and of the thermally annealed rGO (d), rCMGO-1 (e) and rCMGO-2 (f).

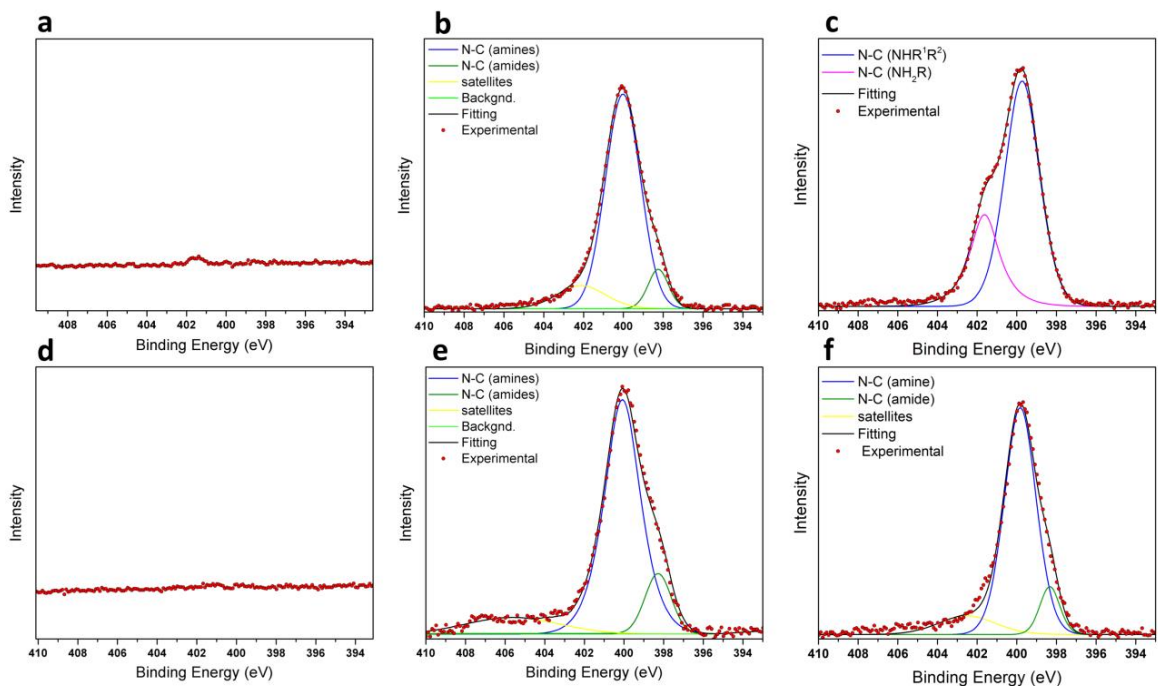


**Figure S2.** XPS spectra of N1s peaks of GO (a), CMGO-1 (b), CMGO-2 (c) and of the thermally annealed rGO (d), rCMGO-1 (e) and rCMGO-2 (f).

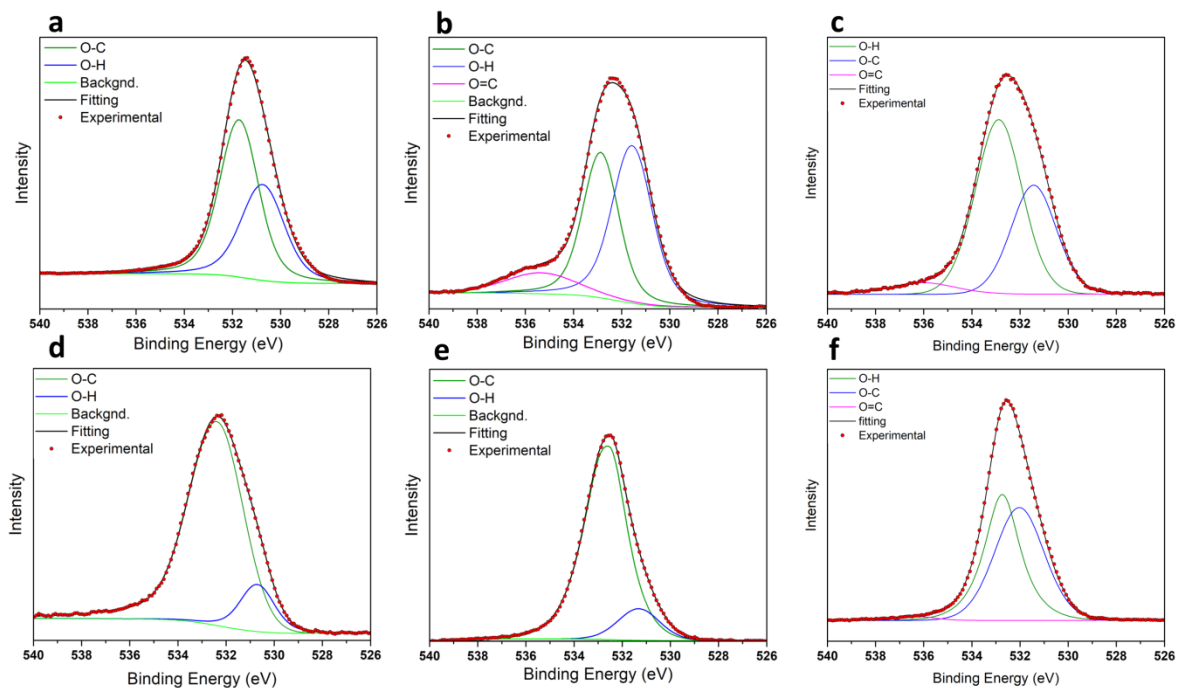


**Figure S3.** XPS spectra of O1s peaks of GO (a), CMGO-1 (b), CMGO-2 (c) and of the thermally annealed rGO (d), rCMGO-1 (e) and rCMGO-2 (f).

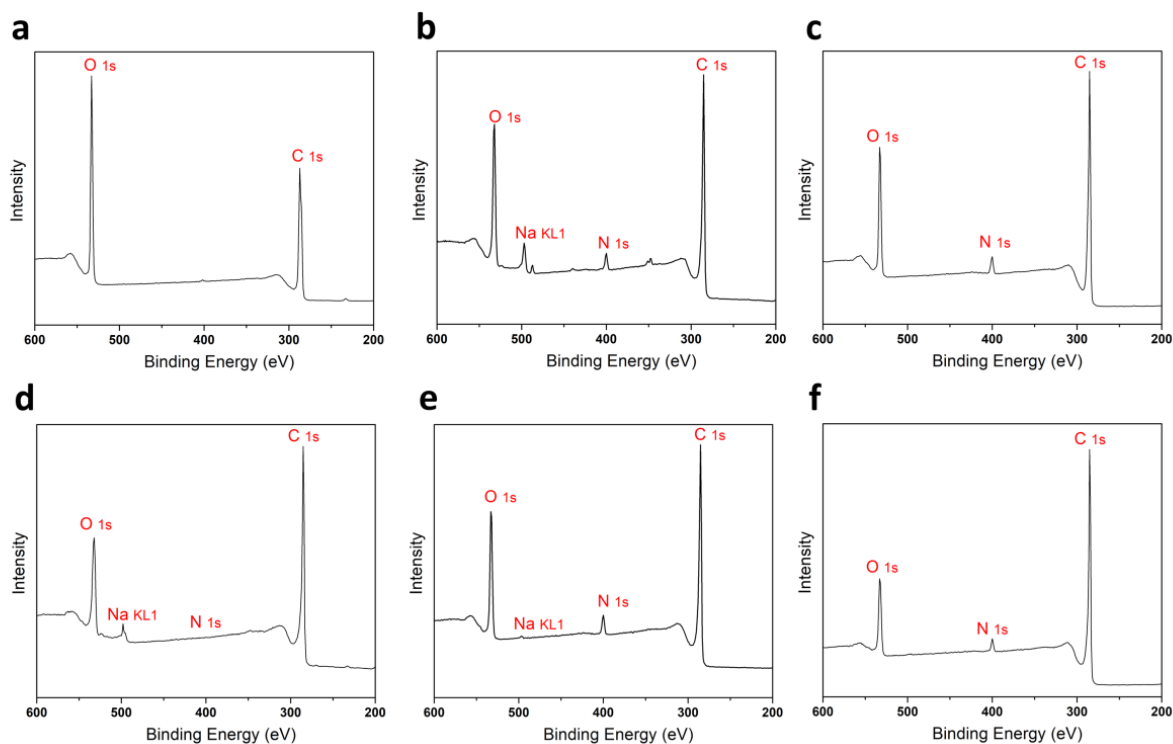


**Figure S4.** XPS survey spectra of GO (a), CMGO-1 (b), CMGO-2 (c), rGO (d), rCMGO-1 (e) and rCMGO-2 (f).

**Table S1:** Elemental atomic abundance of C, N, O obtained from the XPS survey spectra for GO and CMGO before and after the thermal annealing.

	GO	rGO	CMGO-1	rCMGO-1	CMGO-2	rCMGO-2
Element	Atomic %					
C (1s)	67.31	79.97	73.60	75.57	80.66	83.94
N (1s)	0.11	0.14	4.36	4.49	3.75	3.62
O (1s)	32.45	19.59	22.04	19.94	15.58	12.44

### Estimation of the functionalization grade by XPS

The number of NTEG and decylamine molecules in rCMGO-1 and rCMGO-2 per number of carbon atoms of GO was estimated considering that any NTEG or decylamine molecule contributes to the total number of carbon atoms “seen” by the XPS. For any N atom of the NTEG molecule there are 7 C atoms and for any N atom of decylamine there are 10 C atoms. Therefore, the ratio of the number of carbon atoms of graphene over the number of NTEG and decylamine molecules can be expressed as follows:

$$\frac{C_{graphene}}{NTEG\ molecules} = \frac{C\%_{tot} - 7 \times N\%_{tot}}{N\%_{tot}} = \frac{75.57 - 7 \times 4.49}{4.49} = 9.83 \quad (1)$$

$$\frac{C_{graphene}}{decylamine\ molecules} = \frac{C\%_{tot} - 10 \times N\%_{tot}}{N\%_{tot}} = \frac{83.94 - 10 \times 3.62}{3.62} = 13.18 \quad (2)$$

Noteworthy, the abundance of nitrogen in rCMGO-1 and rCMGO-2 differs by 0.8%, which is very close to the XPS detection limit. Therefore, we consider the functionalization degree being nearly identical for both systems. The ratio between the number of carbon atoms of graphene over the number of N-containing aliphatic chains is presented to provide a rough approximation on the structure of the hybrid materials.

## Raman spectroscopy

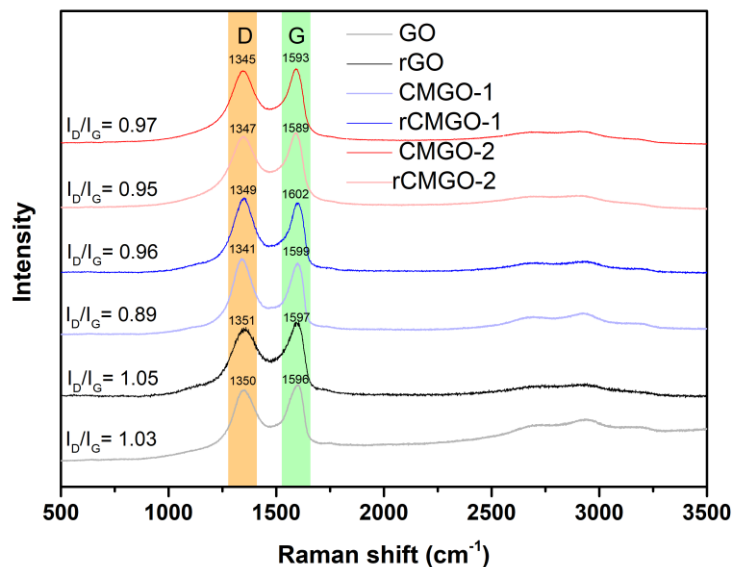


**Figure S5.** Raman spectra of GO, CMGO-1 and CMGO-2 before and after the thermal annealing.

## UV-Vis Transmittance Spectroscopy

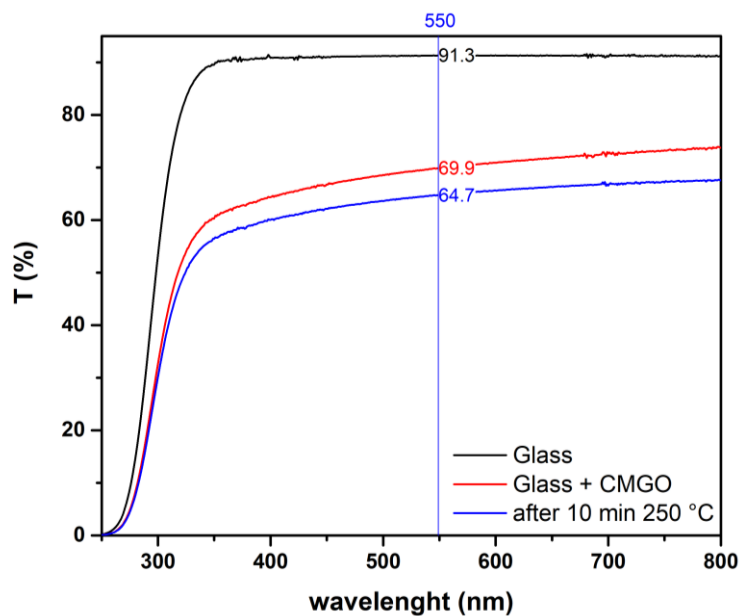


**Figure S6.** Transmittance spectra of the substrate (glass), the substrate with spray-coated CMGO on top before and after the thermal annealing.

## Infrared spectroscopy analysis

The FTIR ATR spectra of the amine NTEG, decylamine, GO, CMGO-1 and CMGO-2 are reported in Figure 2c. The spectrum of GO shows a broad band at  $3390\text{ cm}^{-1}$ , which belongs to the stretching of OH groups of carboxylic and hydroxyl groups and a strong peak at  $1626\text{ cm}^{-1}$  due to the stretching

C=C. The further peaks at 1729, 1213 and 1051  $\text{cm}^{-1}$  correspond respectively to the stretching modes of C=O, C–OH and C–O. The spectrum of NTEG shows a strong peak at 2865  $\text{cm}^{-1}$  due to the stretching of  $\text{CH}_2$ . The two peaks at 3370 and 3307  $\text{cm}^{-1}$  belongs to  $\text{NH}_2$  stretching, while the peak at 1598  $\text{cm}^{-1}$  is characteristic of  $\text{NH}_2$  bending. The peak at 1198  $\text{cm}^{-1}$  is due to C–N stretching. The strong peak at 1098  $\text{cm}^{-1}$  is characteristic of C–O–C stretching.

The spectrum of CMGO-1 shows at 3432  $\text{cm}^{-1}$  the peak corresponding to the stretch of OH. The peaks at 2853  $\text{cm}^{-1}$  and 1084  $\text{cm}^{-1}$  are indicative of the success of the functionalization; in fact, they belong respectively to the stretching of  $\text{CH}_2$  and the stretching of C–O–C introduced by the amine. The spectrum of decylamine shows two strong peaks at 2850 and 2912  $\text{cm}^{-1}$  due to the stretching of  $\text{CH}_2$ . The two peaks at 3332 and 3248  $\text{cm}^{-1}$  belongs to  $\text{NH}_2$  stretching, while the peak at 1568  $\text{cm}^{-1}$  is characteristic of  $\text{NH}_2$  bending. The peak at 1461  $\text{cm}^{-1}$  is due to  $\text{CH}_2$  scissor bending. The spectrum of CMGO-2 shows at 3432  $\text{cm}^{-1}$  the peak corresponding to the stretch of OH. The peaks at 2842  $\text{cm}^{-1}$  and 2913  $\text{cm}^{-1}$  are diagnostic of the success of the functionalization; in fact, they belong to the stretching of  $\text{CH}_2$  of the aliphatic chain. The peak at 1452  $\text{cm}^{-1}$  belongs also to the aliphatic chain and in particular is caused by the bending of  $\text{CH}_2$  groups.

### Thermogravimetric analysis

The thermogravimetric analysis is reported in Figure S8. It is possible to observe that GO presents a first mass loss at 100  $^{\circ}\text{C}$ , the corresponds to the release of the water molecules absorbed, and two more weight loss steps at 150  $^{\circ}\text{C}$  and 260  $^{\circ}\text{C}$  corresponding to the removal of the oxygen-containing functional groups.<sup>4,5</sup> Conversely, CMGO-1 and CMGO-2 are thermally more stable, being already partially reduced during the reaction with the amine. At 60-100  $^{\circ}\text{C}$  they both present a first small mass loss which is again due to the absorbed water and at 185- 190  $^{\circ}\text{C}$  a second, more pronounced mass loss corresponds to the removal of the unreacted oxygen containing groups (in particular hydroxyls) and the effective reduction of CMGOs.<sup>6-9</sup> Finally both CMGOs present a third major weight loss at 320-350  $^{\circ}\text{C}$  that corresponds probably to the elimination of the covalent functionalization and to a higher reduction of graphene.

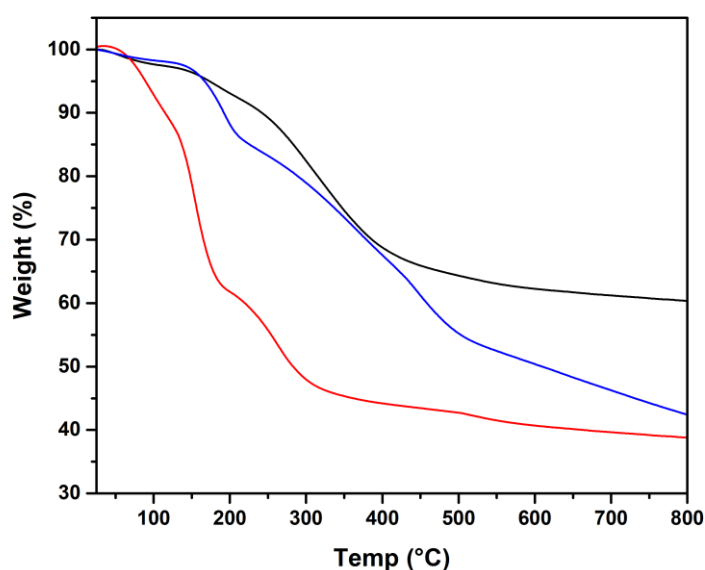


**Figure S7.** Thermogravimetric analysis (TGA) of GO (red), CMGO-1 (black) and CMGO-2 (blue).



## Scanning Electron Microscopy (SEM) characterization

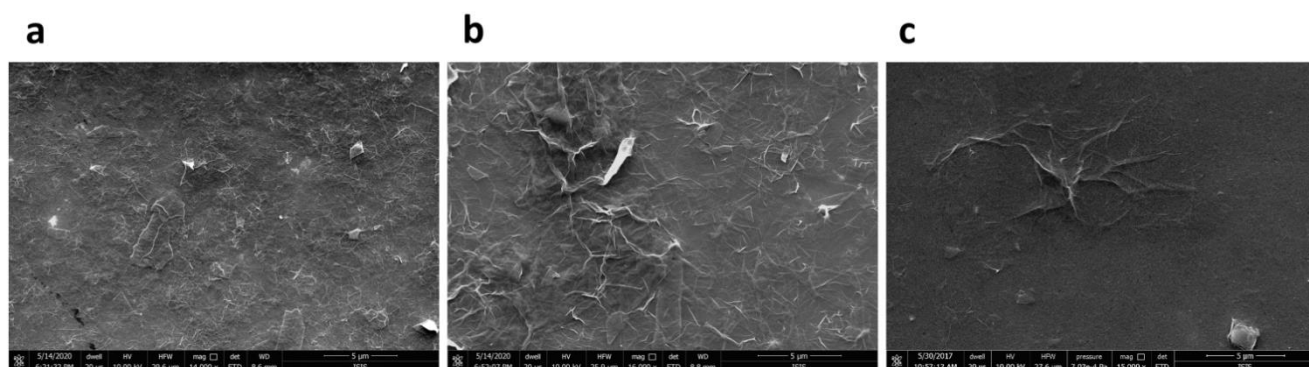


**Figure S8.** SEM images of rCMGO-1(a), rCMGO-2 (b) and rGO(c). The scale bar is 5 μm.

## Atomic Force Microscopy (AFM) characterization

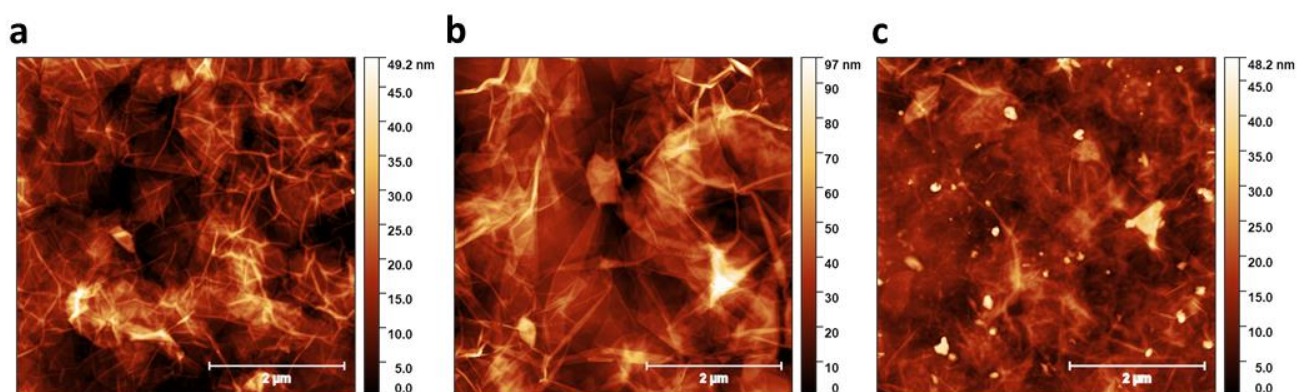


**Figure S9.** AFM images ( 5 μm x 5 μm) of films of rCMGO-1 (a), rCMGO-2 (b) and rGO (c) spray-coated on glass substrates.

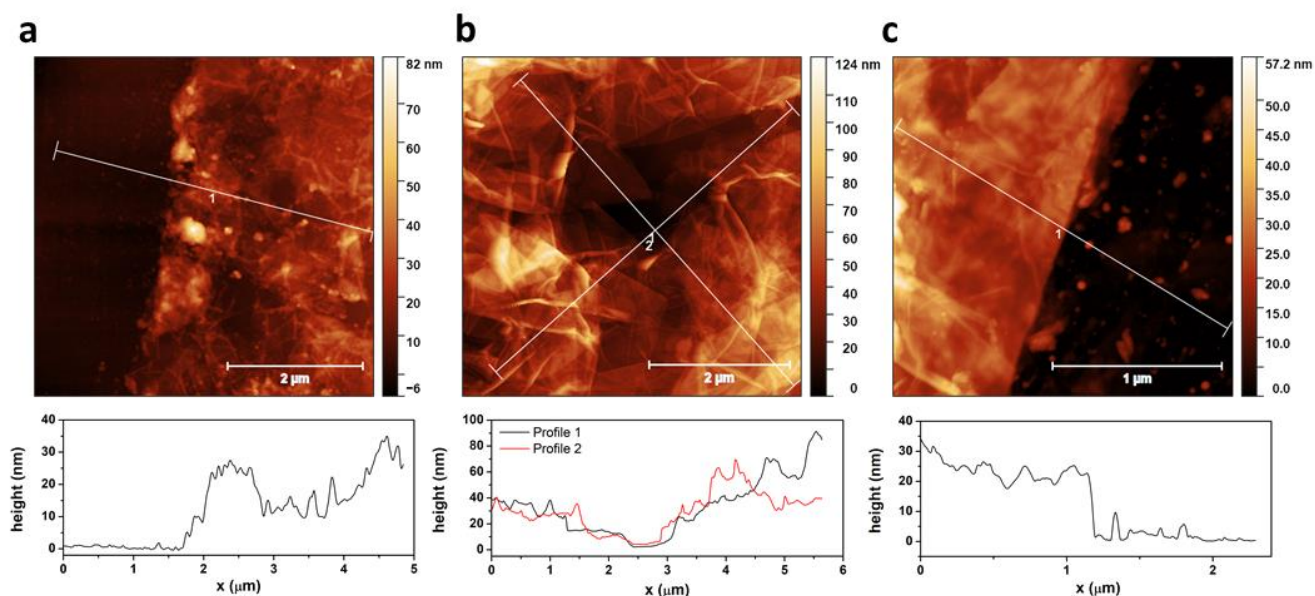


**Figure S10.** AFM images of films of rCMGO-1 (a), rCMGO-2 (b) and rGO (c) in which the substrate is exposed (in a and c the film was mechanically scratched). The corresponding height profiles pointed out in the AFM images are reported under each image.

## Contact Angle

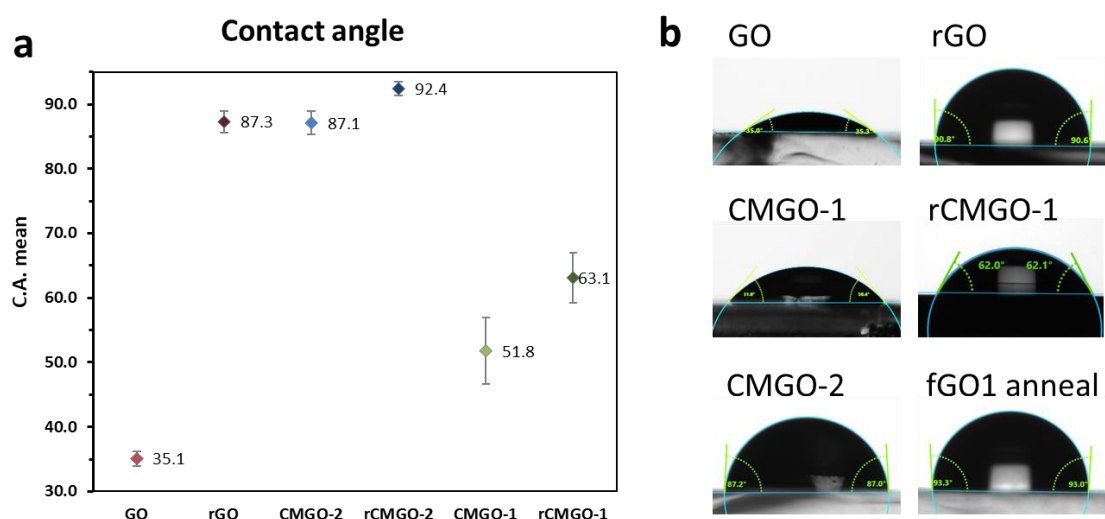


**Figure S11.** Water contact angle measurements. (a) Contact angle of (r)GO, (r)CMGO-1, (r)CMGO-2 and (b) corresponding photos of the water sessile drop on the material with the fitted contact angle represented.

## Humidity sensing and VOC sensing

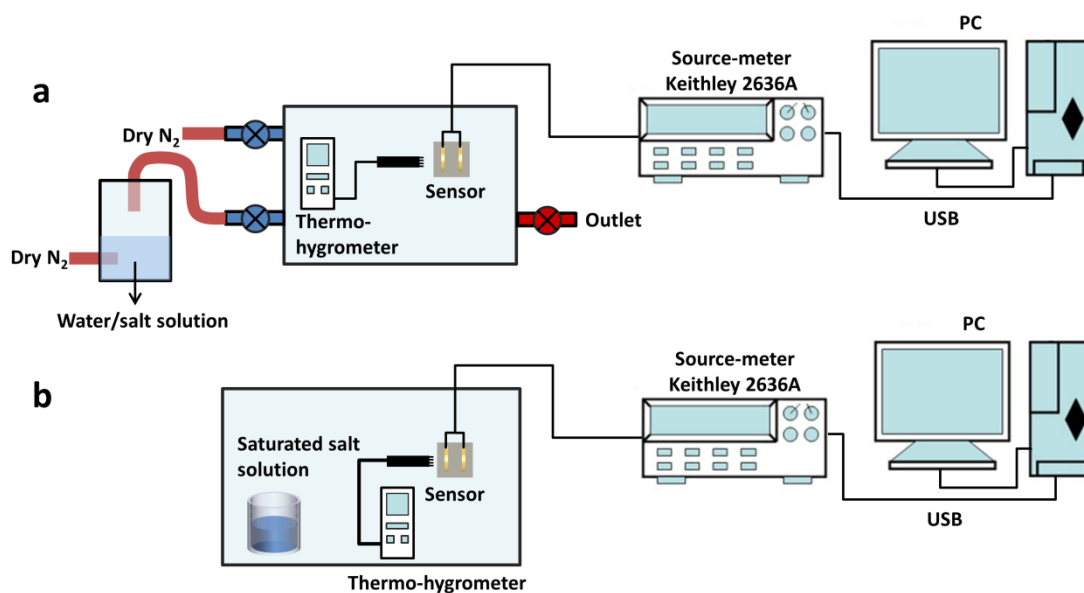


**Figure S12.** Schematic image of the two sensing setup used for the humidity calibration and cycling tests (a) and for the long-term stability test (b).

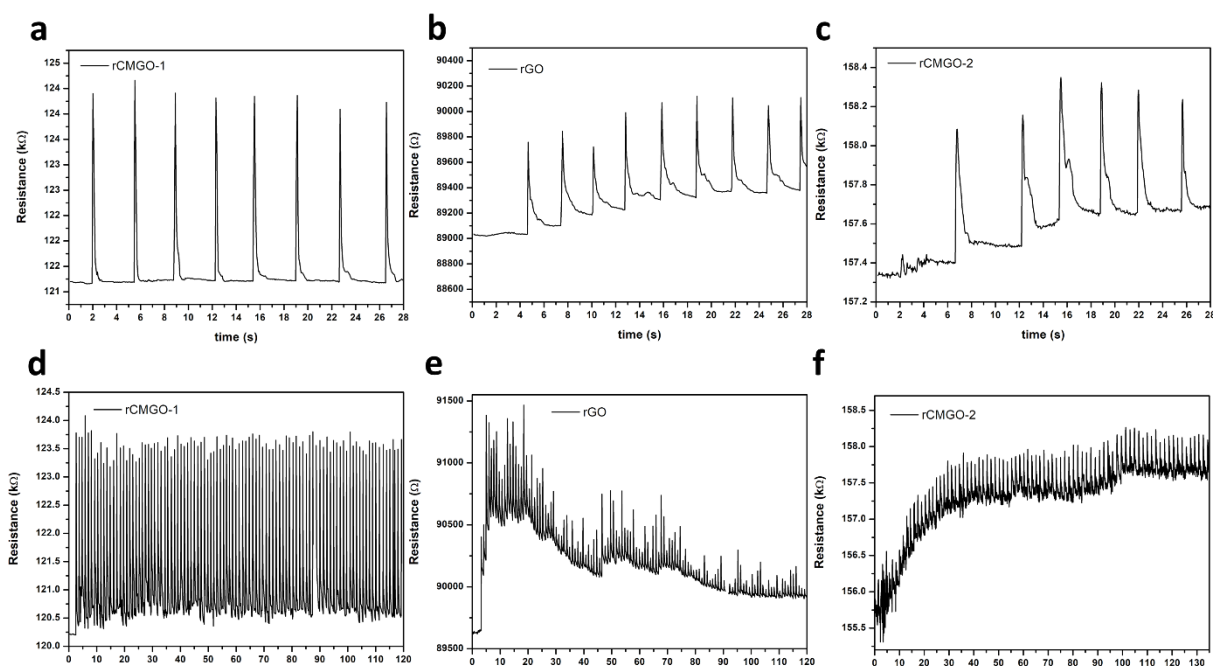


**Figure S14:** Variation of the resistance of the devices rCMGO-1 (a,d), rGO (b,e) and rCMGO-2 (c-f) when the devices are exposed to 100 pulses of humid air during the application of a constant bias of 2 V (a-c) and under a lower number of pulses (d-f)

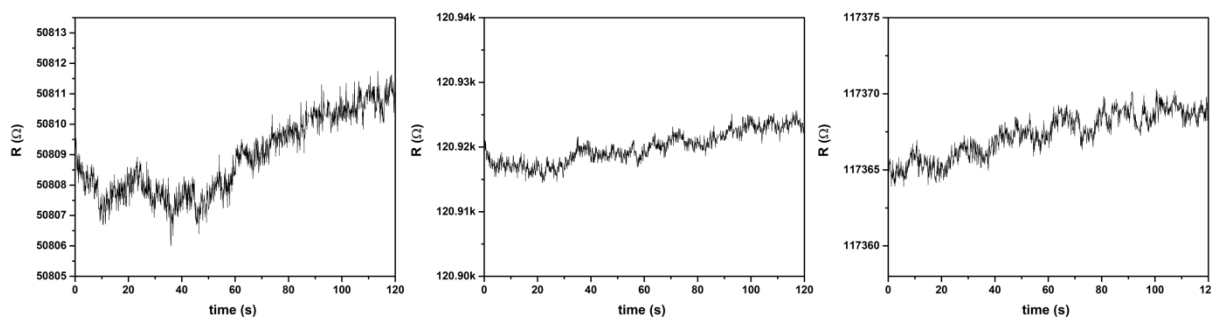


**Figure S13:** Resistance in function of time measured for 3 rCMGO-1 devices during the application of a constant bias of 2V at constant RH (37 %) and constant temperature (24 °C).

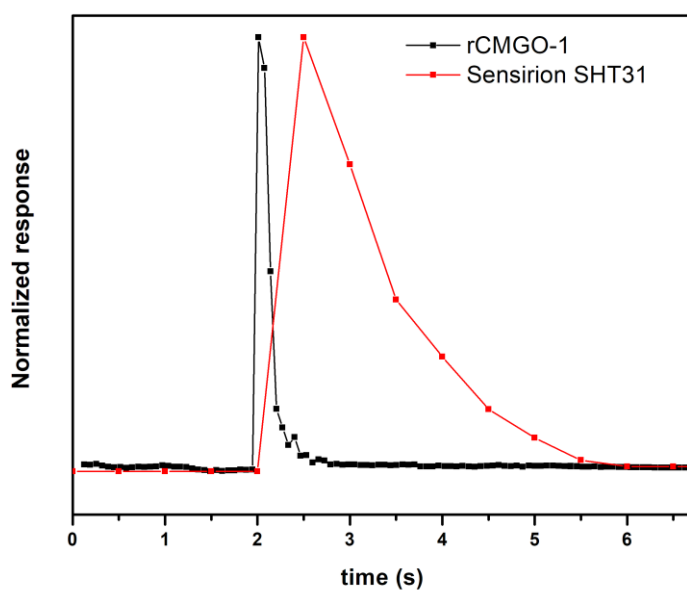


**Figure S15.** Comparison of the normalized responses of rCMGO-1 (black line) and of the commercial sensor Sensirion SHT31 (red line) to the same short pulse of humid air.

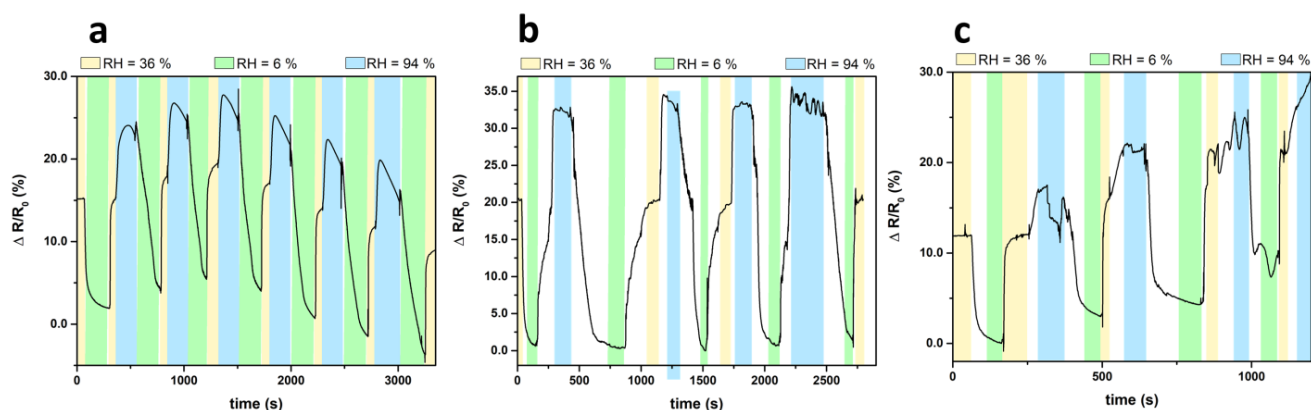


**Figure S16.** Response of the devices (a) rGO, (b) rCMGO-1, and (c) rCMGO-2 as a function of time while the RH was cycled between 6 %, 36 % and 94 %.

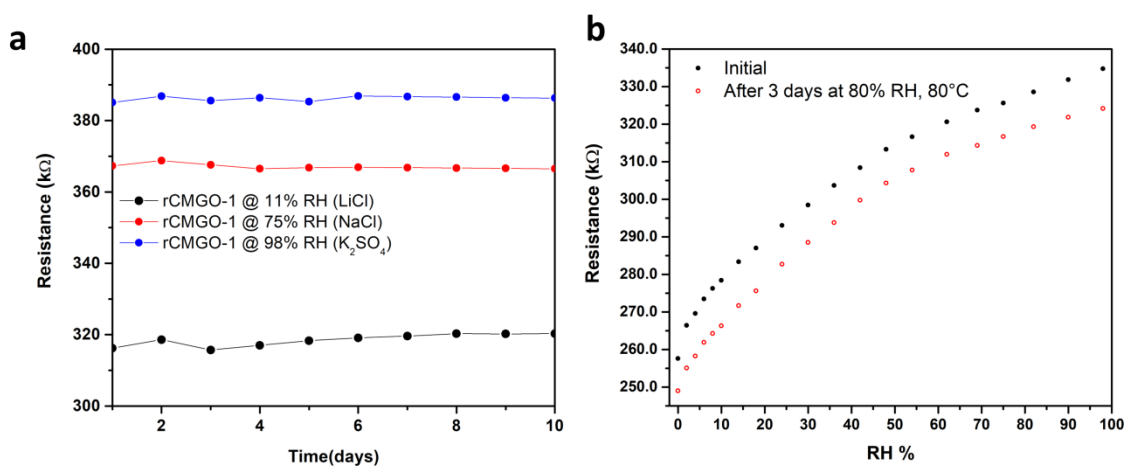


**Figure S17.** Long term stability of rCMGO-1 sensor. (a) Resistance changes over 10 days when the sensor is stored in a low humidity (RH=11%, black dots) and a high humidity (RH=75 %, red dots and RH=98%, blue dots). (b) Resistance in function of the RH of rCMGO-1 sensor before (black dots) and after the exposure to 80 °C at 80 % RH (red empty dots).

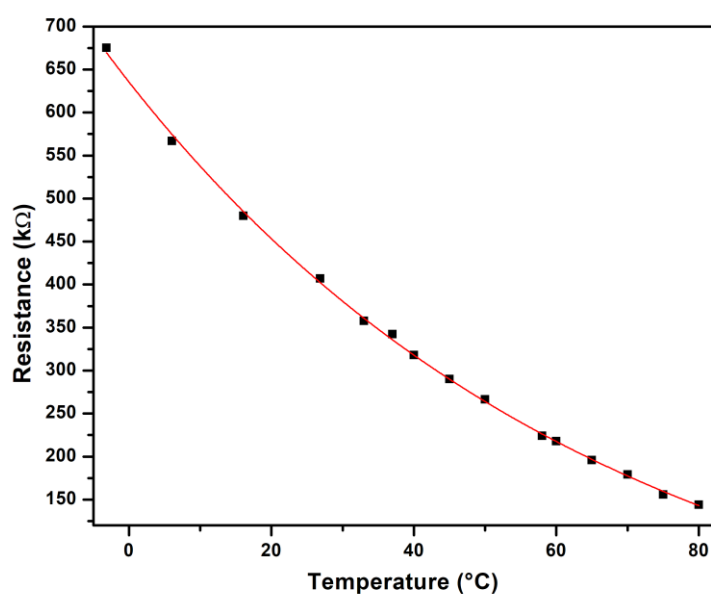


**Figure S18.** Resistance of the rCMGO-1 device in function of the device temperature in the range 0 °C – 80 °C at constant RH = 0%.

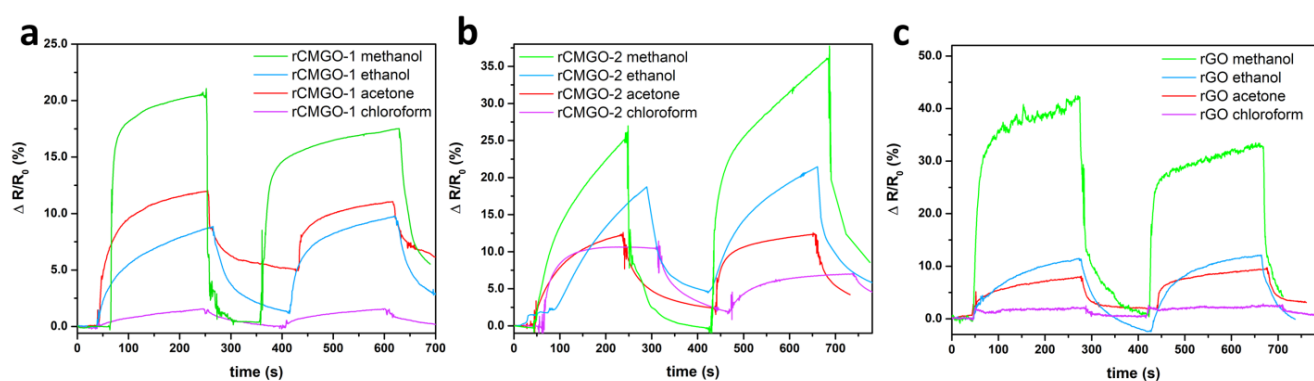


**Figure S19.** Cross sensitivity to VOCs vapors: Cycles of the response in function of time when (a) rCMGO-1, (b) rCMGO-2 and (c) rGO are exposed alternatively to nitrogen and saturated vapor pressure of methanol (green line), ethanol (blue line), acetone (red line) and chloroform (purple line).

**Table S2.** Sensitivity of the three sensors rCMGO-1, rCMGO-2 and rGO to VOCs and water vapor, obtained by normalizing the average response to the analytes for the vapor pressure of each analyte at 20 °C.

	Methanol %(kPa <sup>-1</sup> )	Ethanol %(kPa <sup>-1</sup> )	Acetone %(kPa <sup>-1</sup> )	Chloroform %(kPa <sup>-1</sup> )	Humidity %(kPa <sup>-1</sup> )
<b>rCMGO-1</b>	1.41 ± 0.16	1.51 ± 0.11	0.45 ± 0.03	0.07 ± 0.00	13.30 ± 0.79
<b>rCMGO-2</b>	2.34 ± 0.61	3.19 ± 0.32	0.49 ± 0.01	0.43 ± 0.12	5.58 ± 0.46
<b>rGO</b>	2.81 ± 0.46	2.02 ± 0.08	0.37 ± 0.04	0.12 ± 0.02	6.30 ± 0.84
vapor pressure (kPa) at 20 °C	13.0	5.95	24.47	21.17	2.33

## Interlayer spacing vs relative humidity

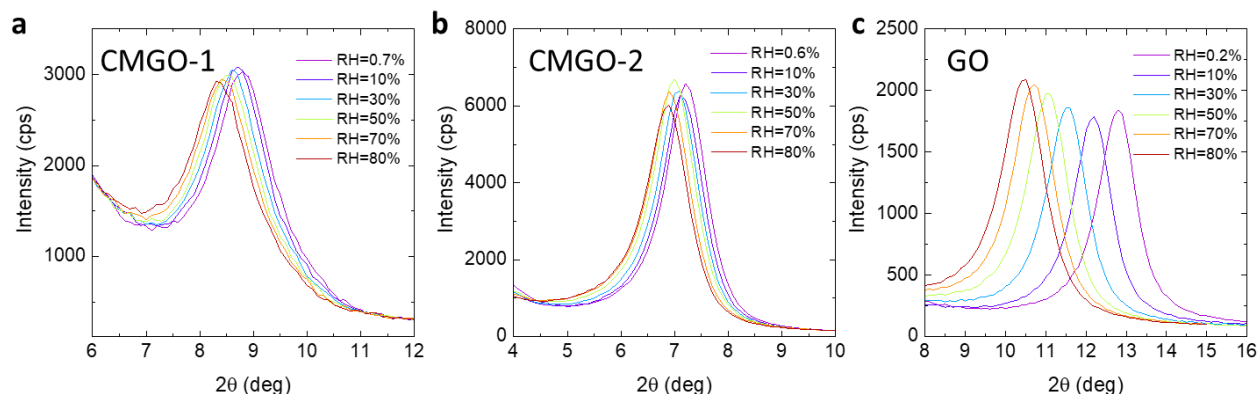


**Figure S20.** XRD patterns of COMGO-1 (a), COMGO-2 (b) and GO (c) recorded in situ during humidity exposure.

XRD patterns carried out on COMGO-1, COMGO-2 and GO samples show a dependence of interlayer spacing from RH (Figure S20). GO spacing strongly increases from 6.93(1) Å to 8.46(1) Å at RH = 80%, as already observed in the literature,<sup>10</sup> due to the intercalation of water molecules, absorbed by hydrophilic sites and then driven through the empty space between non-oxidized regions.<sup>11</sup> Interlayer spacing in dried COMGO-1 and COMGO-2 samples is 10.02(1) Å and 12.24(1) Å, respectively, accordingly to the presence of NTEG and decylamine molecules in stand up configuration. Regardless of the hydrophilicity nature of the functional molecules, water is absorbed and the interlayer spacing increases with RH. The spacing variation is smaller compare to GO sample (Figure S21), probably due to the steric effect of the functional molecules which reduces the free space for water molecules. In contrast, in thermally treated samples, the GO reduction restricts NTEG and decylamine chains in a thinner space leading them to lie down in the basal plane of rCMGOs which, therefore, further shrink the space for water.

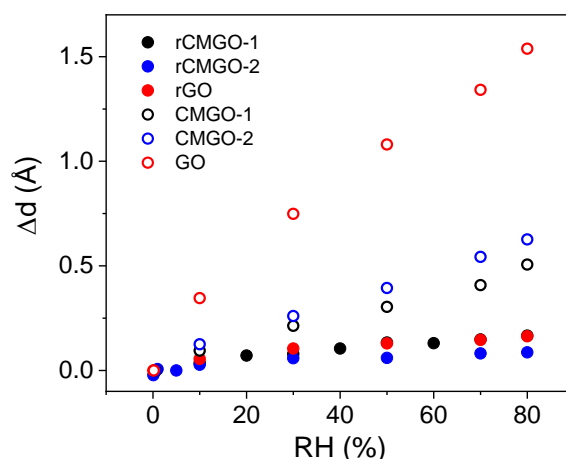


**Figure S21.** Interlayer spacing variation vs. relative humidity. Error bar is smaller than the dot size.



## Molecular Dynamics simulations

CMGO-1 was constructed by grafting 2-[2-(2-methoxyethoxy)ethoxy]ethylamine (NTEG) chains to the graphene layer functionalized with hydroxyl groups, such that, the atomic composition and the surface (density) coverage are identical to that obtained from experimental XPS rCMGO-1 data. To have a quantitative theoretical comparison between rCMGO-1 and rGO/rCMGO-2, the later surfaces were constructed by duplicating CMGO-1 in terms of its density of coverage and atomic composition at the graphene surface. Although the experimental density of coverage (of alkyl chains) of rCMGO-2 is comparable to that of rCMGO-1, two more CMGO structures were constructed by reducing the density of coverage to half of rCMGO-1/ rCMGO-2 (hitherto referred to as rCMGO-1H and rCMGO-2H), such that experimental density of coverage for rCMGO-2 is in between the constructed rCMGO-2 and rCMGO-2H (see Figure S22 and Table S3 for a schematic representation). All of these surfaces were then immersed in a water box containing 9000 water molecules and subjected to molecular dynamics (MD) preparation and sampling runs. Molecular Dynamics (MD) simulations were performed using NAMD software [3] with General AMBER FF [4], employing periodic boundary conditions. For NTEG and decylamine chains, the electrostatic potential fitted (ESP) atomic charges were obtained from quantum-chemical calculations at the MP2/6-311+G(d,p) level of theory using the Gaussian software [5] and these charges between chains and the connected GO surfaces were redistributed following the procedure described in reference [6]. For water, the well-known and reliable “modified TIP3P” force field was used. MD simulations on rGO and rCMGO surfaces were performed in three stages, first, simulations were performed at 100 bar and 300 K (high pressure) for 10 ns to obtain appropriate densities, then simulations were performed in NPT ensemble (1 bar and 300 K) for 10 ns to enable sufficient equilibration of the systems, followed by an MD production run of 50 ns in NPT ensemble. Final MD configurations, taken as an average of 100 MD frames along the 50 ns production run (Figure S23), indicate the presence of de-wetting layer between the water molecules and CMGO-2(H) surface, whereas the water molecules penetrate the surface of rCMGO-1(H), demonstrating the hydrophilic nature of NTEG groups. Mean distance of water molecules measured with respect to the 2D-graphene surface of rCMGOs (see Table S4) also indicate that the penetration of water molecules onto the rCMGO-2 surface is significantly smaller in comparison to that of rCMGO-1(H) surface. Further, Pair Interaction (PI) energy between water molecules and respective rCMGOs and rGO surfaces was computed with the Particle mesh Ewald (PME) grid, using the MD trajectories from the production cycle of 50 ns, to specifically accounting the electrostatic and van der Waals interactions between the respective residues (water-rCMGOs/rGO). Although reduced surface coverage of rCMGO-2 (ie rCMGO-2H surface) enable water penetration onto the surface, the interaction of rCMGO-2 surfaces is significantly smaller in comparison to rCMGO-1(H) and/or rGO surfaces. Subsequently, one water molecule is selected at random and Potential of Mean Force (PMF) profile is computed by lifting the water molecule perpendicular to the surface of rGO and rCMGO surfaces (taking sp<sup>2</sup> surface carbon atoms as reference). The center of mass movement of the water molecule is unconstrained in the ‘XY’ plane (free movement in the plane parallel to the rGO/rCMGO surface), but constrained along the ‘Z’ axis (perpendicular to the rGO and rCMGO surfaces) with 2 Å and 16 Å employed as lower and upper boundaries. PMF profiles were computed using the Adiabatic Biasing Force (ABF) method [7], with 75 ns of MD simulation time. These PMF energy profiles are composed of three distinct regions, (i) repulsive part - where the perpendicular distance ( $d^\perp$ ) between selected water molecule and rGO/rCMGO 2D-graphene surface is  $< 4$  Å, (ii) interacting part – selected water molecules is physisorbed on rGO/rCMGO surfaces and/ or surrounded by the alkyl chain of rCMGOs, such that  $d^\perp$  is in between 4 Å and 14 Å, and (iii) global minima with a PMF energy  $\sim 0$  kcal/mol ( $d^\perp \sim 14$ -16 Å), where the selected water molecule is surrounded by other solvent water molecules (explicit water). The adsorption, trap, barrier and desorption energies of water molecules with rCMGO surfaces is computed

and is reported in Figure S24 and Table S5. The adsorption energy of water molecules on the rGO/rCMGO surfaces is the relative PMF energy at the local minimum ('mechanical' water trap, taken at  $d^\perp \sim 4 \text{ \AA}$ ) with respect to the global minimum (taken at  $d^\perp \sim 18 \text{ \AA}$ ). Trap energy ( $E_T$ ) is the relative energy required by the water molecule to overcome the local energy barrier associated with the mechanical trap. rCMGO-1(H) surfaces also tend to show an additional local PMF minimum at  $d^\perp \sim 6 \text{ \AA}$ , reflecting the interaction between water molecules and the NTEG-oxygen atoms, characterized by a local energy barrier ( $E_b$ ). Such a local minimum is not observed for rCMGO-2(H) surfaces. Desorption energy ( $E_{\text{Ads}} + E_T$ ) indicates the ease of desorption of water molecules from rGO/rCMGO surface, owing to the repulsive PMF profile. An ideal sensing device with strong response, fast response and short recovery times is that of a system with a set of discrete micro-states, observed in the PMF energy profile, maximizing the differential of the response measured and that can be converted with relatively low energy barriers from ON to OFF and vice-versa. Clearly, rCMGO-1 (See Fig: S24) fulfills this condition (with a set of discrete states with low barrier heights), hence enabling fast dynamics and response (ON and OFF). To elucidate the 'comparatively' strong response of rCMGO-1 surface, we quantified the orientation of the 'selected' water molecule in the micro-states: 'A' & 'C' as indicated in Figure S25 – left image. The relative orientation of the water molecule with respect to Z axis (perpendicular to rCMGO-1/2 surface) is computed by taking the three angles based on the vectors passing through atoms in the selected water molecule: O-H1, O-H2 and H1-H2, wherein 'O', 'H1' & 'H2' are atoms of a selected water molecule. The acute angle between O-H1, O-H2, H1-H2 and Z axis for rCMGO-1 and rCMGO-2 surfaces, in positions 'A' & 'C' are indicated in Table S6. In positions A & C (micro-states, see Figure S24 - left image), water molecule in rCMGO-1 shows a specific orientation, whereas rCMGO-2 shows some orientation only in position A, as indicated in Figure S26 and Table S6. rGO and rCMGO-2 surfaces on the other hand does not show any such orientation. A quasi-continuous ensemble of microstates is therefore observed for rGO (and to a lesser extent in rCMGO-2H at reduced coverage), wherein the orientation of water is more isotropic, as is the case of any 'selected' water molecule in liquid water. Therefore, a set of discrete micro-states with low energy barriers and a constrained orientation of water molecule at the micro-states - offer a plausible explanation to the fast and strong response of rCMGO-1 surface to the water molecules, compared to rGO and rCMGO-2H surfaces.

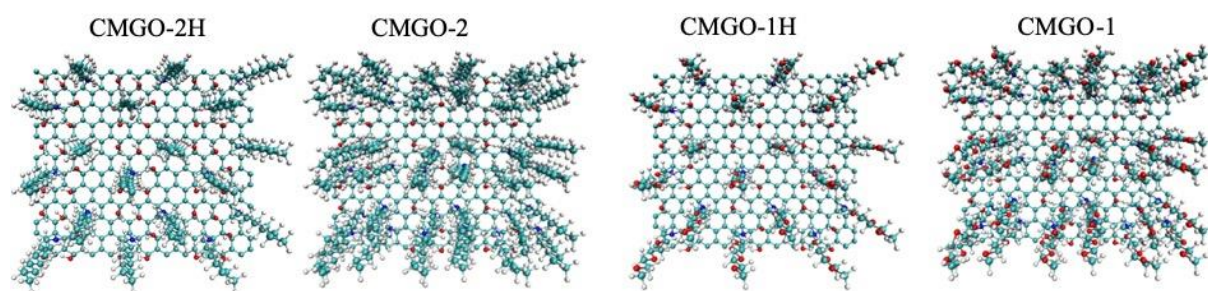


**Figure S22.** Schematic representation of rCMGO surfaces considered for MD simulations.



**Table S3:** Atomic composition (in %) considered for MD simulations. Atomic composition (and the corresponding density of surface coverage) of rCMGO-1 and rGO are taken with reference to the experimental XPS data (Table 1). rCMGO-2 is constructed to contain the same density of coverage of rCMGO-1, for quantitative theoretical comparisons.

Atomic composition (%)					
Element/Name	rGO	rCMGO-2H	rCMGO-2	rCMGO-1H	rCMGO-1
C	80.0	88.1	90.0	87.0	75.0
O	20.0	8.5	5.0	9.25	20.0
N	0.0	3.4	5.0	3.75	5.0
C/N	0.0	26.0	18.0	23.5	15.0

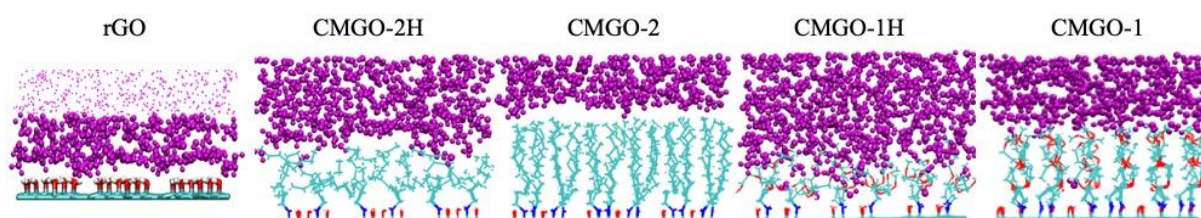


**Figure S23.** Final MD configurations of rGO and rCMGO surfaces, taken as the average of 100 MD frames along the production cycle. A dewetting layer can be observed for rCMGO-2(H) surface (indicating hydrophobic nature), whereas the water molecules are able to penetrate the rCMGO-1(H) surface, demonstrating its hydrophilic nature in comparison to rCMGO-2(H) surfaces.

**Table S4.** The average distance of water molecules from the graphene surface. The distances are computed as the mean of 100 MD frames taken over 50 ns of production cycle.

Name	Height (Å)	Distance: water (Å)
rCMGO-2	$14.31 \pm 0.17$	$15.07 \pm 0.31$
rCMGO-1	$13.22 \pm 0.34$	$10.17 \pm 2.61$
rCMGO-2H	$10.19 \pm 0.65$	$8.47 \pm 1.27$
rCMGO-1H	$10.77 \pm 0.63$	$5.11 \pm 2.32$

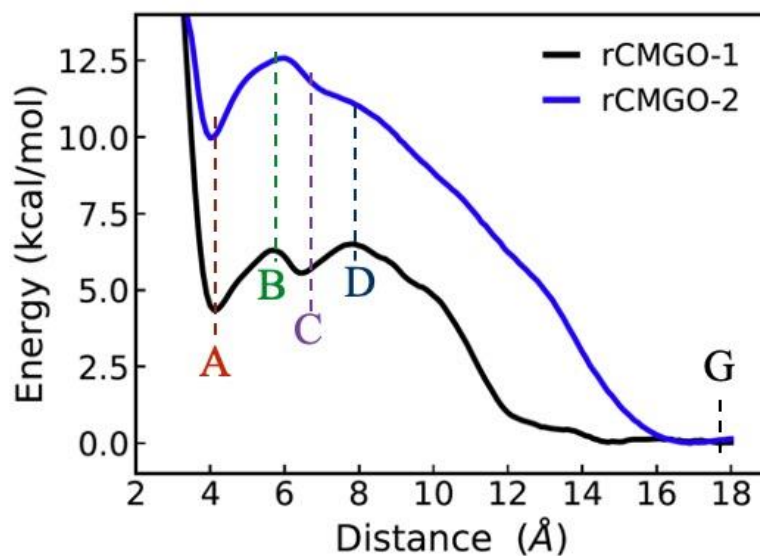


**Figure S24.** PMF adsorption profile of water molecule with rCMGO-1 and rCMGO-2 surfaces, reflecting the adsorption, trap, barrier and desorption energies with their characteristic local and global minimum. Relative energies are reported in Table 4.

**Table S5.** Adsorption energy ( $E_{\text{ads}}$ ) of a water molecule on rGO/rCMGO surfaces and  $E_{\text{T}}$  and  $E_{\text{b}}$  correspond to the PMF trap and barrier energies.

Name	$E_{\text{Ads}}$ ( $E_{\text{A}}-E_{\text{G}}$ )	$E_{\text{Dis}}$ ( $E_{\text{B}}-E_{\text{G}}$ )	$E_{\text{T}}$ ( $E_{\text{B}}-E_{\text{A}}$ )	$E_{\text{b}}$ ( $E_{\text{C}}-E_{\text{D}}$ )
rGO	0.35	0.54	0.19	0.05
rCMGO-2	9.94	12.55	2.61	--
rCMGO-1	4.27	6.07	1.80	0.81
rCMGO-2H	2.71	2.96	0.25	--
rCMGO-1H	2.63	3.15	0.52	0.20

Desorption energy ( $E_{\text{Dis}}$ ) is the sum of  $E_{\text{ads}}$  and  $E_{\text{T}}$ , indicative of the ease of desorption of water molecules from the rGO/rCMGO surface. All energies are computed with respect to Figure 12 and are reported in the units of kcal/mol.

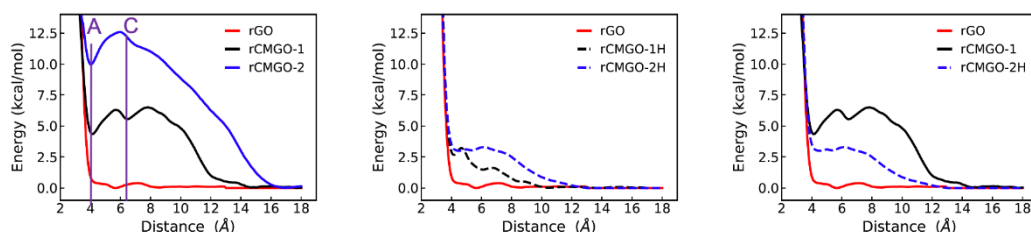


**Figure S25:** PMF adsorption profile of water molecule with rGO, rCMGO-1 and rCMGO-2 surfaces, reflecting the adsorption, trap, barrier and desorption energies with their characteristic local and global minimum. Set of discrete microstates in rCMGO-1 and rCMGO-2 are indicated by 'A' and 'C' in the left image.

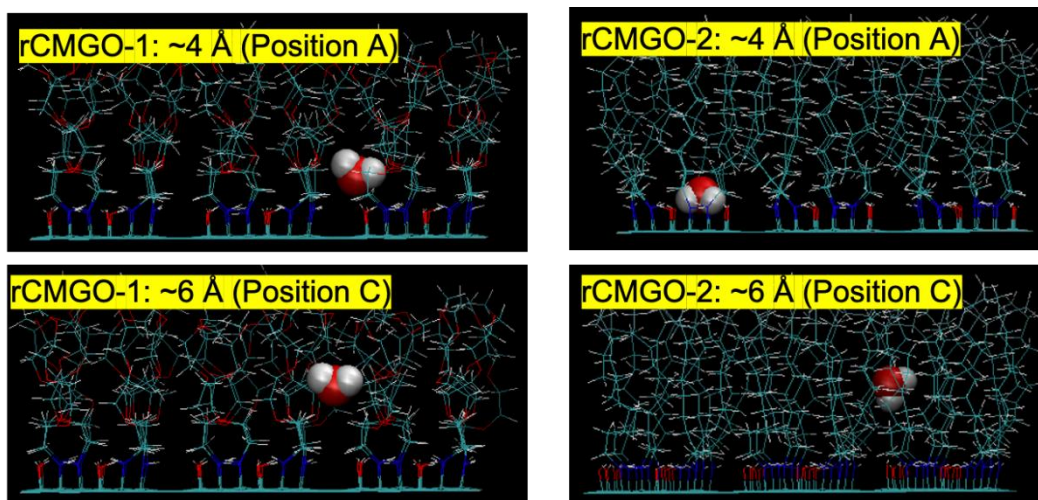


**Figure S26:** Orientation of water molecule at positions A & C for rCMGO-1 and rCMGO-2 surfaces. Positions ‘A’ and ‘C’ are taken with respect to Fig S24, wherein the center-of-mass distance of selected water molecule from the GO surface is  $\sim 4\text{\AA}$  and  $\sim 6\text{\AA}$ , respectively.

**Table S6:** Acute angle formed by the vectors passing through the atoms (O, H1 and H2) of a selected water molecule: O-H1, O-H2, H1-H2 and Z axis (perpendicular to rCMGO-1/2 surface) for rCMGO-1 and rCMGO-2 surfaces, in positions ‘A’ and ‘C’ as indicated in Fig 13. In liquid water, the angles between O-H1, O-H2, H1-H2 and Z-axis are  $\sim 0 \pm 40$ , indicating an isotropic orientation of water molecules.

Surface	Moiety/Vector	Angle at Position A	Angle at Position C
rCMGO-1	O-H1	$61 \pm 11$	$72 \pm 15$
	O-H2	$63 \pm 10$	$70 \pm 14$
	H1-H2	$87 \pm 10$	$88 \pm 10$
rCMGO-2	O-H1	$21 \pm 31$	$10 \pm 26$
	O-H2	$25 \pm 30$	$12 \pm 25$
	H1-H2	$75 \pm 21$	$20 \pm 30$

## <sup>1</sup>H NMR of the molecule NTEG

<sup>1</sup>H NMR (400 MHz, Chloroform-*d*) δ 3.68 – 3.62 (m, 6H), 3.55 (dd, *J* = 5.7, 3.6 Hz, 2H), 3.51 (t, *J* = 5.2 Hz, 2H), 3.38 (s, 3H), 2.86 (t, *J* = 5.2 Hz, 2H).

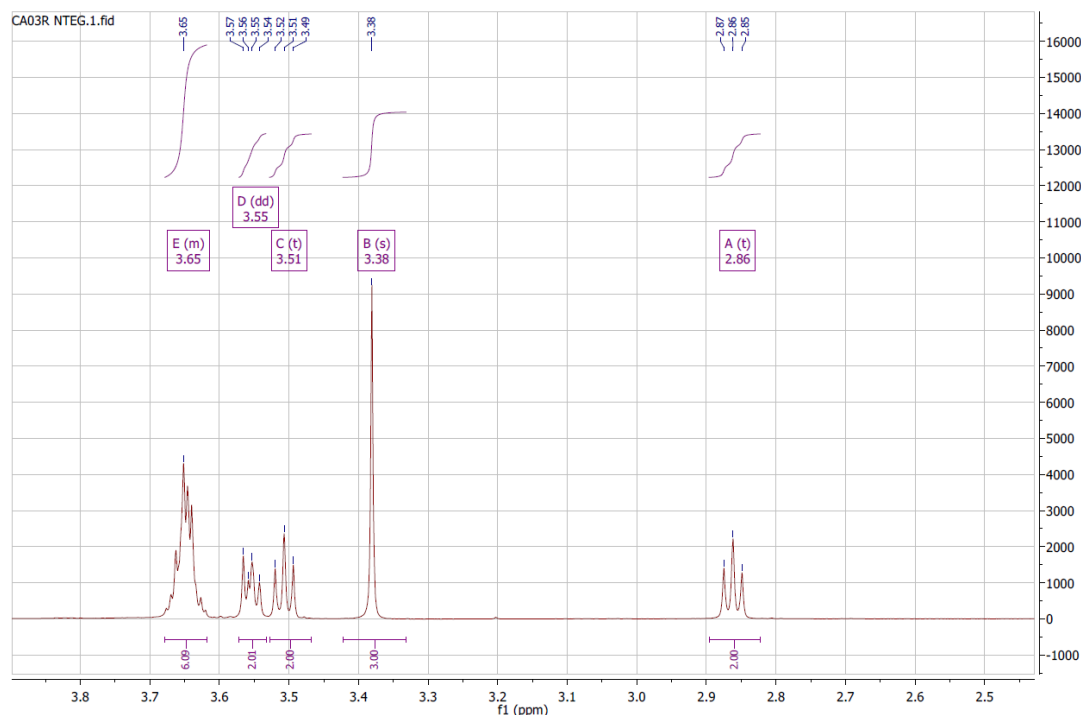


**Figure S27:** <sup>1</sup>H-NMR of the synthesized NTEG molecule.

## References

1. Park, K. D.; Liu, R.; Kohn, H. Useful Tools for Biomolecule Isolation, Detection, and Identification: Acylhydrazone-Based Cleavable Linkers. *Chem. Biol.* **2009**, *16* (7), 763-772.
2. Kim, H.; Kang, Y. J.; Jeong, E. S.; Kang, S.; Kim, K. T. Glucose-Responsive Disassembly of Polymersomes of Sequence-Specific Boroxole-Containing Block Copolymers under Physiologically Relevant Conditions. *ACS Macro Lett.* **2012**, *1* (10), 1194-1198.
3. Greenspan, L. Humidity fixed points of binary saturated aqueous solutions. *J. Res. Natl. Bur. Stand. Sect. A Phys. Chem.* **1977**, *81 A* (1), 89-96.
4. Wu, T.; Wang, X.; Qiu, H.; Gao, J.; Wang, W.; Liu, Y. Graphene oxide reduced and modified by soft nanoparticles and its catalysis of the Knoevenagel condensation. *J. Mater. Chem.* **2012**, *22* (11), 4772-4779.
5. Hsiao, M.-C.; Ma, C.-C. M.; Chiang, J.-C.; Ho, K.-K.; Chou, T.-Y.; Xie, X.; Tsai, C.-H.; Chang, L.-H.; Hsieh, C.-K. Thermally conductive and electrically insulating epoxy nanocomposites with thermally reduced graphene oxide-silica hybrid nanosheets. *Nanoscale* **2013**, *5* (13), 5863-5871.
6. Acik, M.; Lee, G.; Mattevi, C.; Pirkle, A.; Wallace, R. M.; Chhowalla, M.; Cho, K.; Chabal, Y. The Role of Oxygen during Thermal Reduction of Graphene Oxide Studied by Infrared Absorption Spectroscopy. *J. Phys. Chem. C* **2011**, *115* (40), 19761-19781.
7. Bagri, A.; Mattevi, C.; Acik, M.; Chabal, Y. J.; Chhowalla, M.; Shenoy, V. B. Structural evolution during the reduction of chemically derived graphene oxide. *Nature Chem.* **2010**, *2* (7), 581-587.
8. Slobodian, O. M.; Lytvyn, P. M.; Nikolenko, A. S.; Naseka, V. M.; Khyzhun, O. Y.; Vasin, A. V.; Sevostianov, S. V.; Nazarov, A. N. Low-Temperature Reduction of Graphene Oxide: Electrical Conductance and Scanning Kelvin Probe Force Microscopy. *Nanoscale Res. Lett.* **2018**, *13* (139), 1-11.
9. Tegou, E.; Pseiropoulos, G.; Filippidou, M. K.; Chatzandroulis, S. Low-Temperature Thermal Reduction of Graphene Oxide Films in Ambient Atmosphere: Infra-Red Spectroscopic Studies and Gas Sensing Applications. *Microelectron. Eng.* **2016**, *159*, 146-150.
10. Cervený, S.; Barroso-Bujans, F.; Alegria, A.; Colmenero, J. Dynamics of Water Intercalated in Graphite Oxide. *Journal of Physical Chemistry C* **2010**, *114* (6), 2604-2612.
11. Nair, R. R.; Wu, H. A.; Jayaram, P. N.; Grigorieva, I. V.; Geim, A. K. Unimpeded Permeation of Water Through Helium-Leak-Tight Graphene-Based Membranes. *Science* **2012**, *335* (6067), 442-444.